






# A 4096 channel event-based multielectrode array with asynchronous outputs compatible with neuromorphic processors

**Working Paper****Author(s):**

Cartiglia, Matteo; Costa, Filippo; [Narayanan, Shyam](#) ; [Bui, Cat Vu Huu](#) ; Ulusan, Hasan; Risi, Nicoletta; Haessig, Germain; Hierlemann, Andreas ; [Cardes Garcia, Fernando](#) ; [Indiveri, Giacomo](#) 

**Publication date:**

2023-10-24

**Permanent link:**

<https://doi.org/10.3929/ethz-b-000655539>

**Rights / license:**

[Creative Commons Attribution 4.0 International](#)

**Originally published in:**

Research Square, <https://doi.org/10.21203/rs.3.rs-3468607/v1>

**Funding acknowledgement:**

188910 - Deciphering Neuronal Networks: Advancing Technology and Model Systems (SNF)

# A 4096 channel event-based multielectrode array with asynchronous outputs compatible with neuromorphic processors

Matteo Cartiglia<sup>1,\*</sup>, Filippo Costa<sup>1</sup>, Shyam Narayanan<sup>1</sup>, Cat-Vu H. Bui<sup>2</sup>, Hasan Ulasan<sup>2</sup>, Nicoletta Risi<sup>3</sup>, Germain Haessig<sup>1</sup>, Andreas Hierlemann<sup>2</sup>, Fernando Cardes<sup>2</sup>, and Giacomo Indiveri<sup>1</sup>

<sup>1</sup>Institute of Neuroinformatics, University of Zurich and ETH Zurich, Switzerland

<sup>2</sup>Department of Biosystems Science and Engineering, ETH Zurich, Switzerland

<sup>3</sup>Groningen Cognitive Systems and Materials Center, University of Groningen, Netherlands

\*camatteo@ini.uzh.ch

## ABSTRACT

Bio-signal sensing represents a pivotal domain in the medical applications of bioelectronics. Traditional methods have, so far, focused on capturing these signals as accurately as possible, leading to high sampling rates in clocked synchronous architectures. Given the sparse activity of bio-signals, this approach often results in large amounts of digitized data with no relevant information and in a significant amount of energy consumed during transmission. Here, we introduce a self-clocked microelectrode array (MEA) that senses and digitizes bio-signals at the pixel level by encoding their changes as asynchronous digital address-events, significantly reducing the amount of data that needs to be transmitted off-chip. This novel MEA comprises an array of  $64 \times 64$  electrodes, an asynchronous 2D-arbiter, and an Address-Event Representation (AER) communication block. Each pixel within the array operates autonomously, monitoring input signals for relative voltage fluctuations instigated by cellular activity. Upon detecting a sufficiently large signal change, the pixel produces a digital pulse encoded with its corresponding address. Positive signal changes are encoded as “up” events, while negative ones are encoded as “down” events and, upon generation, are routed off-chip instantly via the asynchronous arbiter. Here, we present results from the chip characterization and experimental measurements using electrogenic cells. Moreover, we interface the MEA to a mixed-signal neuromorphic processor, demonstrating a prototype for end-to-end event-based bio-signal sensing and processing.

## 1 Introduction

2 As we usher in an era of pervasive computing, we are witnessing an exponential proliferation of devices and systems designed  
3 to aid us in our daily lives. These systems are very diverse, ranging from localization devices to biomedical sensors. Still, they  
4 are all expected to operate continuously at minimal energy cost while facing the daunting task of ensuring the secure real-time  
5 interpretation of the generated data. This is especially true in the realm of biosensors that continuously monitor our bodily state  
6 through various signals. These include neural signals, manifested as action potentials and measured by electroencephalogram  
7 (EEG), cardiac signals manifested as extracellular field potential and recorded as electrocardiogram (ECG), as well as glucose  
8 and insulin signals. The current data inundation from these sensors necessitates the development of custom hardware that  
9 can process signals locally without the need for offline bulky backend computers or cloud servers. Biosensors, particularly  
10 those with many channels such as the ones employed in electrophysiological studies such as multielectrode arrays (MEAs),  
11 are experiencing a trend towards higher channel counts, for simultaneous recording from as many as 235k channels [1]. If  
12 encoded using a classical digital sampling approach, the bio-signal measured by a typical channel produces about 200kbps,  
13 making scalability and off-chip transmission critical in terms of both bandwidth and power consumption [1–7]. Although  
14 innovations in recording systems, such as time-multiplexing techniques and sophisticated sampling schemes, have allowed for  
15 simultaneous recording from an increasingly large number of electrodes, the practical scalability of these systems remains  
16 difficult. Furthermore, most electrophysiology studies are primarily interested in the timing and shape of action potentials.  
17 Consequently, a considerable portion of the acquired data ends up being discarded only *after* costly post-processing techniques.  
18 This highlights the need for more efficient data acquisition and processing techniques that can better focus on the features of  
19 interest *on-line*, ultimately enabling more efficient on-line and closed-loop bio-signal processing systems [8].

20 In parallel, neuromorphic sensors [9–13] have emerged as a paradigm-shifting solution for low-latency and power-efficient

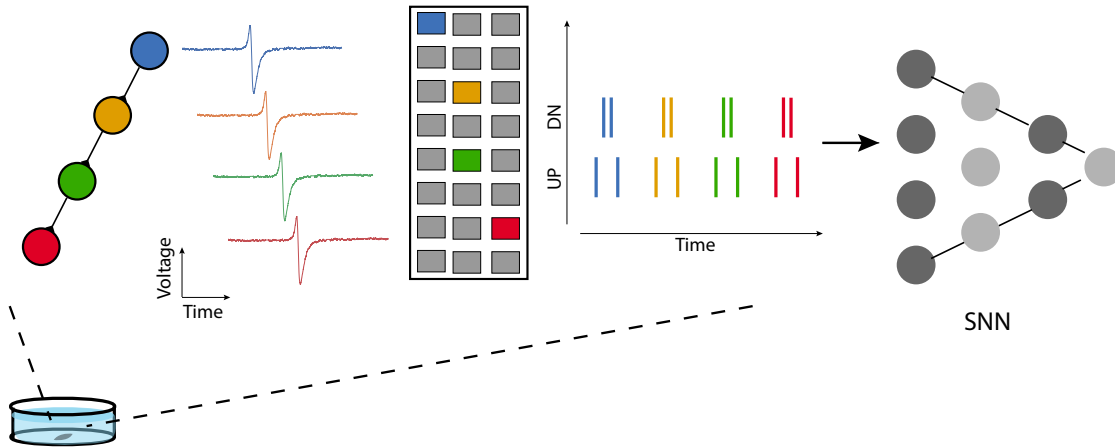


**Figure 1. Schematic overview of GAIA’s operating principle and benefits.** Graphical representation of the working principle of the event-based 4096-channel GAIA sensor. The signal is sensed and compressed at the pixel level, enabling sparse and compressed data transmission off-chip. The new data topology is particularly well suited for online processing with Spiking Neural Networks (SNN).

21 signal processing. Unlike traditional sensing technologies that output a continuous, clocked stream of data, neuromorphic  
 22 sensors are asynchronous and event-driven. Event-based sensors only respond to significant changes in the signal, thus  
 23 drastically reducing data traffic and, subsequently, power consumption. Their clock-less, or self-clocked, operation bypasses  
 24 the power-hungry high-frequency clock requirements, making them well suited for real-world edge, pervasive, and ubiquitous  
 25 computing applications. Furthermore, when neuromorphic sensors are synergistically paired with neuromorphic processors [14–  
 26 17], they unlock unprecedented potential, enabling sophisticated real-time signal processing [18] that can handle high temporal  
 27 resolution requirements [19, 20], rapid pattern recognition [21, 22], and adaptive learning, challenges [23] that traditional  
 28 systems often struggle with.

29 Within this context, in this paper, we present a fully event-based microelectrode array biosensor called GAIA (Global  
 30 Asynchronous Intelligent Array). The GAIA system uses neuromorphic circuits to encode signals generated from bioelectric  
 31 cells directly at the pixel level, generating and transmitting data only when relevant events, such as an action potential, occur.

32 Here, we first introduce the GAIA chip architecture, characterize the circuitry within each pixel, and characterize the  
 33 signal encoding block (level-crossing ADC). We then demonstrate the ability of the sensor to detect bioelectric signals, and,  
 34 finally, we validate GAIA with a beating cardiomyocyte culture. Going a step further, we interface GAIA to a mixed-signal  
 35 event-based neuromorphic processor, demonstrating a proof-of-principle end-to-end neuromorphic sensing and processing  
 36 pipeline. Figure 1 outlines the full event-based pipeline: time-continuous sensing, sparse asynchronous event generation, and  
 37 finally, spike-based processing. This novel combination represents an important step toward achieving an efficient, scalable,  
 38 and adaptable sensing system that elegantly captures the spatio-temporal dynamics of biological systems while at the same time  
 39 significantly reducing the amount of data transmitted off-chip.

## 40 Results

41 GAIA’s distinct advantage lies in its adaptive data transmission approach: by outputting an asynchronous digital event only  
 42 when detecting a local relative voltage change that surpasses a preset threshold, it favors the encoding of meaningful biological  
 43 signals with large transients and discards noise and small fluctuations. Intuitively, our approach is based on the assumption that  
 44 relevant biological signals exhibit voltage transients significantly higher than the noise floor. This unique data handling strategy  
 45 makes the output data solely dependent on the detected activity of the signal, and since the activity of bioelectric cells is sparse  
 46 in both space and time, it significantly reduces the overall output data [24].

### 47 The event-based microelectrode array

48 Figure 2a shows an overview of the 4096-channel GAIA MEA system. It consists of a central  $64 \times 64$  pixel core, flanked  
 49 by two X and Y address encoders, and an Address Event Representation (AER) [25] communication block. Each electrode

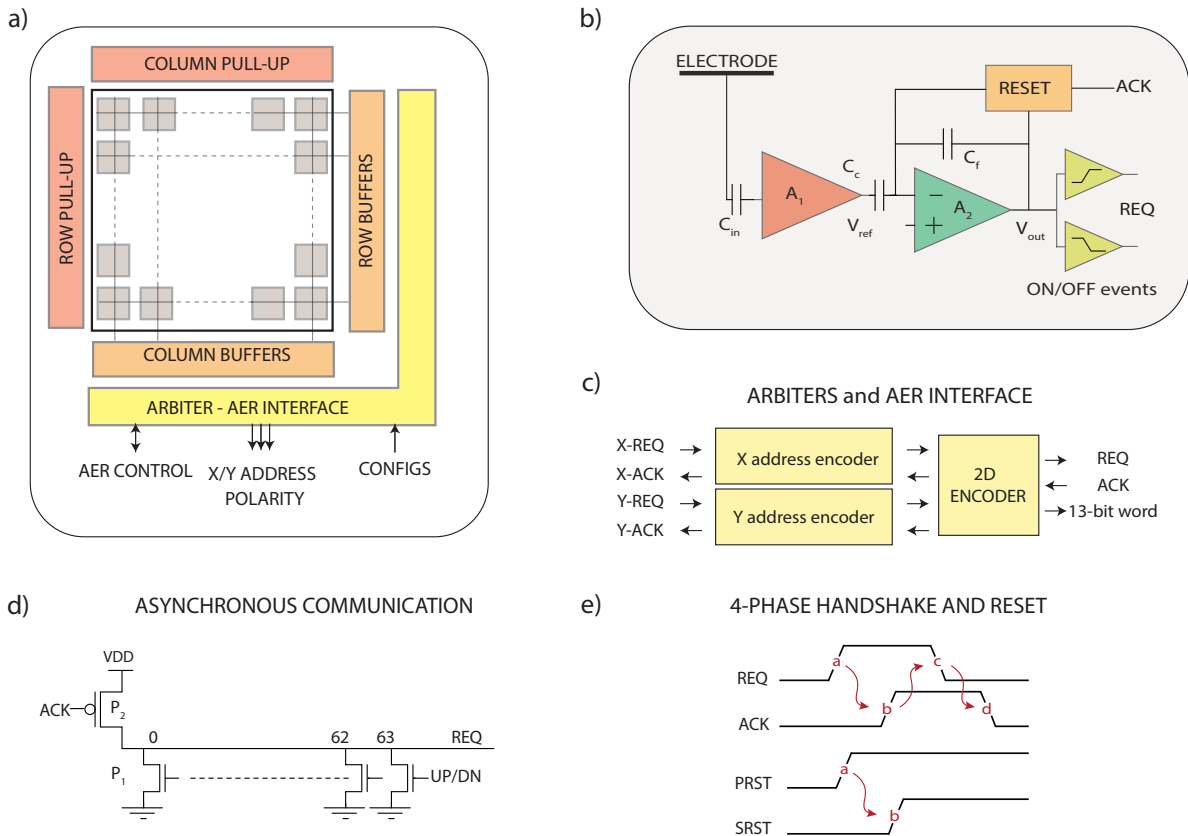


**Figure 2.** Detailed breakdown of the CMOS GAIA event-based microelectrode array. **a**, High-level system architecture depiction. **b**, Close-up view of the circuit elements within each pixel. **c**, A schematic diagram illustrating the arbiter and address event representation hierarchy. **d**, Core asynchronous communication components showing pull-up and pull-down transistors, responsible for generating and transmitting Request (REQ) and Acknowledgment (ACK) signals. **e**, Temporal sequence of the 4-Phase handshake protocol fundamental to asynchronous communication on top. On the bottom the sequence of reset signals.

50 measures  $15 \times 15 \mu\text{m}^2$ , and the pitch between electrodes is  $48 \mu\text{m}$ . Figure 2b shows a block diagram of the signal path within  
51 each pixel: it includes two adjustable gain stages (A1-A2), an event generation stage, and a reset stage. A large reference  
52 electrode,  $10 \mu\text{m}$  in width, is positioned on the perimeter of the sensing array.

53 The A1-A2 amplifiers were designed to amplify signals in the 1Hz-10kHz range while rejecting the large DC component at  
54 the electrode-tissue interface. The amplitude of signals of interest can vary considerably and typically have amplitudes that  
55 range from  $50 \mu\text{V}$  to  $1 \text{mV}$  depending on the distance to the electrode and the cell type. The initial amplification stage (A1 - in  
56 red in figure 2b) is a single-ended common-source amplifier in which the gain is regulated by an adjustable current source. A  
57 tunable gate in the pseudo-resistor modifies the low cutoff frequency corner [26]. The pseudo-resistor in A1, working with the  
58  $C_{in}$  capacitor, establishes a very low-frequency pole, stabilizing the original zero. The signal is subsequently AC-coupled to  
59 a variable gain amplifier (A2 - in green in figure 2b), where the  $C_c/C_f$  ratio determines the gain, offering eight configurable  
60 settings. Further details of the circuitry within each pixel are available in the supplementary material 1.

61 The event generation block (in yellow in figure 2b) emits two digital types of events (UP and DN), depending on the  
62 direction of the signal variations [27]. These are linked to a four-phase asynchronous handshaking block, managing data  
63 transmission through asynchronous signals. Generated UP or DN pulses correspond to AER interface requests (REQ). The  
64 REQ signal will elicit an acknowledgment (ACK) signal from the downstream processing, resetting the comparator output.

### 65 **Arbiter and address–event representation (AER) interface**

66 Each channel is integrated within an array. This array communicates asynchronously with peripheral circuits through a  
67 handshaking mechanism [25, 28, 29]. Upon event generation, the pixel raises a request signal (REQ) indicating its readiness for  
68 data transmission [30, 31]. A 2D-arbiter system encodes this event’s location using a unique (X,Y) address and event polarity  
69 (ON or OFF). This results in a 13-bit digital address: 6-bit each for X and Y addresses, complemented by an ON/OFF polarity  
70 bit. The structure of this 2D arbitrator can be seen in Figure 2c.

71 To ensure a smooth handshaking process, the target receiver verifies all digital REQ events created on the chip. These signals  
72 employ a Bundled Data (BD) representation, where the 13-bit digital address is portrayed as a parallel word. This word is then  
73 accompanied by two supplementary REQ and ACK signals for handshaking control. The timing scheme of the asynchronous  
74 four-phase handshake, as well as the timing of the reset signals, is shown in Figure 2e. In scenarios where multiple pixels  
75 simultaneously produce Address Events (AEs), the arbitration block comes into play to prevent signal interference. This block  
76 sequentially queues and transmits events over a shared bus, ensuring a collision-free environment. The peak throughput of the  
77 GAIA system is measured to be 20 mega events per second (Meps).

78 Figure 2d elucidates the method through which each pixel accesses this shared bus. To relay data, a pixel pulls the shared  
79 REQ line to ground, using a local pull-down transistor, signaling the need for event transmission. Recognizing this action, the  
80 downstream arbiter returns an ACK signal to a global pull-up transistor within the common line, thereby resetting the REQ  
81 signal. This allows for subsequent event transmissions.

82 To enhance system fairness and efficiency, we adopted a 2D non-greedy arbiter [32, 33]. Such arbiters strive to allocate  
83 equal access to the shared bus among competing nodes. The principle is simple: an arbiter will not acknowledge the same  
84 client consecutively, only proceeding after all other waiting clients have been attended to. This approach increases fairness,  
85 minimizes potential system congestion, and improves the overall performance of the system.

### 86 **Characterization of amplifier gain, noise, power consumption, and latency.**

87 The electrical properties of GAIA were characterized by applying a  $1 \text{mVpp}$  sinusoidal input and sweeping its frequency from  
88  $0.1 \text{Hz}$  to  $10 \text{kHz}$ . Figure 4a illustrates the transfer functions that characterize the A1-A2 amplifier chain for various gain  
89 settings. The lowest and middle gain settings yield in-band amplifications of  $37.4 \text{dB}$  and  $48.1 \text{dB}$ , respectively. The gain can be  
90 programmed up to  $57 \text{dB}$ . Additionally, by altering the bias of the A1 pseudo-resistor, the high-pass corner can be changed. We  
91 characterized the noise levels of the chip by sweeping the input frequency and amplitude using a spectrum analyzer. Figure 4b  
92 displays the signal-to-noise-distortion ratio (SNDR) as a function of the input amplitude. The dynamic range for the lowest  
93 gain setting is  $37.9 \text{dB}$ , with a peak SNDR of  $37.2 \text{dB}$ . Moreover, figure 4c demonstrates the power spectral density (PSD) of  
94 the input-referred noise across GAIA’s operational bandwidth. The integrated input-referred noise in the  $500 \text{Hz} - 3 \text{kHz}$   
95 band is  $19.04 \mu\text{V}$ , while in the full  $5 \text{Hz} - 10 \text{kHz}$  bandwidth is  $71.05 \mu\text{V}$ .

96 The power consumption of a single pixel is  $842.4 \text{nW}$ . Figure 4d illustrates the contributions from various pixel structures.  
97 The analog and digital components within the pixel are supplied separately; the amplifiers are supplied with analog power  
98 (in blue), while the digital structures within the pixel receive digital power (in red). The total power consumption of the chip,  
99 including the pixel core and the 2D arbiter, amounts to  $3.58 \text{mW}$ . Figure 4e displays the breakdown for each power supply.  
100 Power calculations were performed using nominal biases, with a  $2 \text{kHz}$  event rate response from each pixel.

101 The pixel response latency was assessed by measuring a single pixel’s response to a low-frequency square wave. The sensor  
102 generates a positive event on every rising edge and a negative event on every falling edge. Figure 4f displays the latency for  
103 both positive and negative events. The average latency is  $0.9995 \mu\text{s}$ , and the 1-sigma response jitter is  $0.2798 \mu\text{s}$ . As expected,

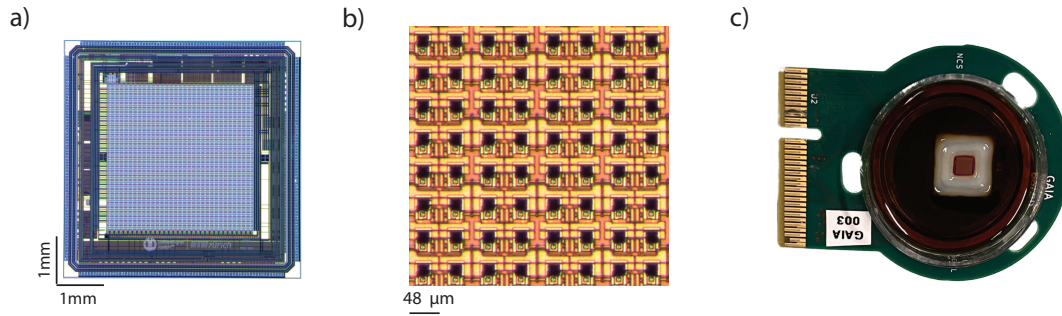


**Figure 3.** **a**, Micrograph showcasing the GAIA chip with dimensions of a  $5 \times 5 \text{ mm}^2$  die and an active area of  $3 \times 3 \text{ mm}^2$ . **b**, Microscope image of the post-processed electrode array. The electrodes have a size of  $15 \times 15 \mu\text{m}^2$  and are spaced squarely with a pitch of  $48 \mu\text{m}$ . A small area of  $4 \times 6$  electrodes is highlighted: the exposed top electrode is visible. **c**, Image of the finalized, fully-packaged chip. Following post-processing, the chip was affixed to a daughterboard PCB, encapsulated using a biocompatible epoxy resin, and subsequently coated with Pt-black to minimize electrode impedance.

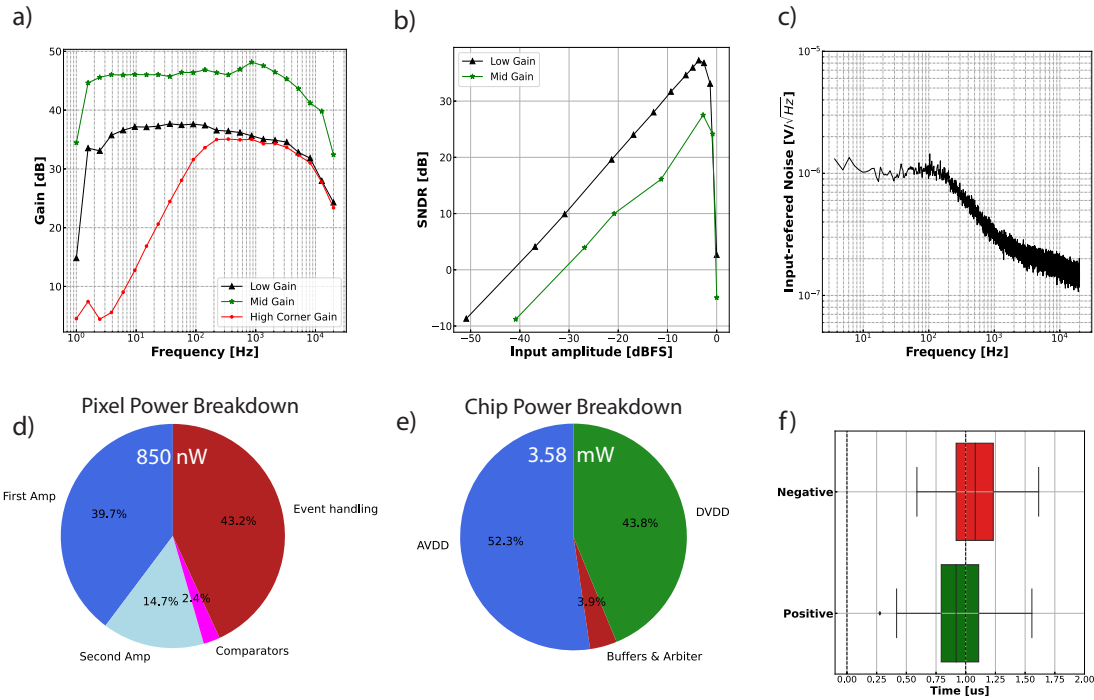


**Figure 4. Electrical Characterization of the GAIA Microelectrode Array.** **a**, Transfer functions of the A1-A2 amplifier chain across different gain settings. The amplifier offers eight programmable gain levels: the lowest (illustrated in black) is at 37.4 dB, the middle (shown in green) at 48.1 dB, and the high-pass filter corner can be adjusted (highlighted in red) via the A1 pseudo-resistor bias settings. **b**, Signal-to-noise-distortion ratio (SNDR) plotted against input amplitude. At the lowest gain setting (depicted in black), the dynamic range is 37.9 dB with an SNDR of 37.2 dB. **c**, Power spectral density representing the input-referred noise over the operational bandwidth of GAIA. Notably, the integrated input-referred noise within the 500 Hz-3 kHz range amounts to  $19.04 \mu\text{V}$ . **d**, Detailed breakdown of power consumption for individual structures within a single pixel. Power sources for analog and digital components are depicted in blue and red, respectively. The total power consumption is 842.4 nW per pixel. **e**, Comprehensive power consumption analysis for each power supply, resulting in an overall chip consumption made up of 3.58 mW. **f**, Assessment of response latency for both positive and negative events, with an average latency measured at 0.9995 us.

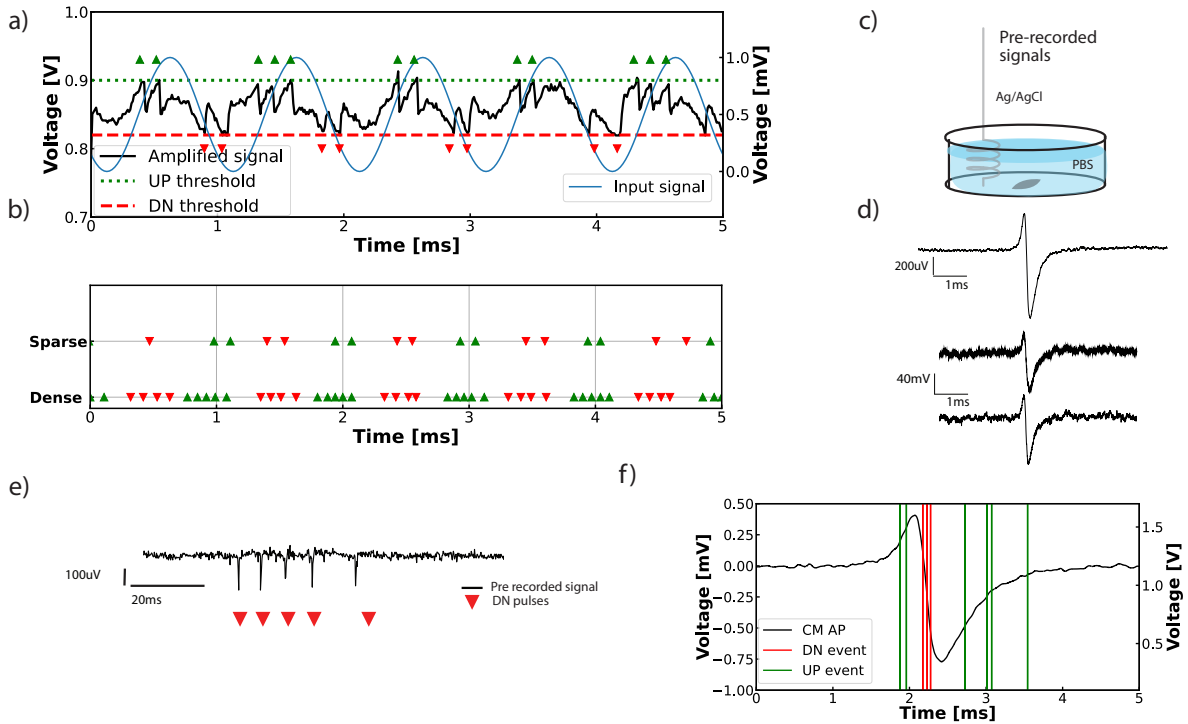


**Figure 5. Event Characterization of the GAIA Microelectrode Array.** **a**, Encoding of a 1 kHz sine wave. The original waveform (in blue) is amplified (in black) by the A1-A2 amplifier chain. When the amplified signal crosses the upper threshold (in green) or falls below the lower threshold (in red), positive or negative events are triggered, respectively. After crossing a threshold, the amplified signal is reset to a reference voltage, allowing the AC dynamics to persist. **b**, The density of events can be influenced by the width of the thresholds, resulting in either denser (bottom) or sparser (top) event patterns. **c**, Experimental setup employed to assess GAIA with bioelectric signals. A function generator is connected to an Ag/AgCl electrode submerged in PBS (Phosphate Buffer Saline) solution. **d**, Previously recorded cardiomyocyte extracellular field potential (top) and its corresponding sensed and amplified signal through the GAIA amplifier chain. **e**, DN events (bottom in red) produced in response to a pre-recorded neural signal (top in black). **f**, UP (in green), and DN events (in red) produced in response to a single pre-recorded cardiomyocyte extracellular field potential.

104 positive events exhibit lower latency than negative events due to design choices within the pixel. For layout symmetry purposes,  
 105 the comparators are designed using transistors of the same size. Positive events are generated from an n-FET-based comparator  
 106 (with electrons as majority carriers), while negative events are produced from a p-FET-based comparator (with holes as majority  
 107 carriers). The lower mobility of holes compared to electrons causes the pFET comparator to switch more slowly, resulting in  
 108 higher latency for events with negative polarity. Characterizing latency using a single pixel is also valid for the larger array, as  
 109 the pixel's response time is assumed to be orders of magnitude larger than the propagation time of digital events through the  
 110 gates of the arbiter tree.

### 111 Event characterization

112 Following the initial electrical and functional characterization of GAIA, we characterized the event generation encoding at the  
 113 core of the innovation of GAIA.

114 Figure 5a presents the Asynchronous Delta Modulator (ADM) encoding of a 1 kHz sine wave. The original sine wave,  
 115 single-channel events, amplified signal, and event-generating thresholds are all superimposed. A digital UP (DN) event is  
 116 produced when the amplified signal exceeds (falls below) a configurable threshold, resetting the amplified signal to A2's  
 117 positive output terminal. The placement of thresholds can be freely adjusted. Intuitively, the closer the thresholds, the more  
 118 events will be generated, resulting in a denser or sparser encoding of the original signal. Figure 5b shows a 1 kHz sine wave  
 119 encoded with different degrees of sparsity. Given known thresholds, the precise timing of the UP/DN events produced by the  
 120 event-generating ADM circuitry contains all the information about the original input signal [27, 34] (Signal reconstruction is

121 available in the Supplementary Material section 4). To ensure our approach is effective, we aim to position the thresholds above  
122 the noise level to only capture large extracellular signals.

123 To fully characterize the on-chip amplification and event generation of GAIA, we tested the system using previously  
124 recorded signals. A function generator was connected to a silver-silver chloride electrode, which was submerged in phosphate-  
125 buffered saline (PBS) solution and positioned inside GAIA's recording chamber. Figure 5c illustrates the setup. The conductive  
126 PBS solution allows the signal from the function generator to be detected by all electrodes on the array. Using a previously  
127 recorded signal allowed us to test GAIA's response to a real extracellular potential through the electrode signal pathway and the  
128 entire encoding pipeline.

129 Figure 5d displays a previously recorded cardiomyocyte extracellular field potential (top) and the same signal amplified  
130 by GAIA's A1-A2 amplifiers (bottom). The top trace was previously recorded using another MEA [7] platform and used  
131 to evaluate the GAIA system. Figure 5f demonstrates the event encoding response for the same cardiac extracellular field  
132 potential signal. The extracellular field potential's stereotypical waveform is effectively encoded into an asynchronous stream  
133 of UP-DN-UP events on the chip. Figure 5e shows the response of GAIA to previously recorded neural signal. The neuronal  
134 signal (on top) and the corresponding response of the DN channel (on bottom) are displayed. The pixel accurately detects the  
135 input spike trains, demonstrating the capability of the system to encode and transmit biologically relevant signals.

## 136 Experimental results

137 To rigorously validate the GAIA platform, we recorded from a cardiomyocyte culture. Cardiomyocytes generate periodic  
138 signals [35–37] (at 1Hz), making them exemplary candidates for characterizing novel MEA systems.

139 Human-induced pluripotent stem cells (hiPSC) differentiated into cardiomyocytes were used for this validation process.  
140 Cardiomyocytes were seeded onto the GAIA sensor and kept in a humidity-controlled incubator. Recordings began on day  
141 seven after plating, providing sufficient time for the cells to aggregate and synchronize their beating patterns spontaneously.  
142 Throughout multiple days of observation, the cell culture remained stable, displaying a beating frequency that ranged from 50  
143 to 90 beats per minute (bpm). The main outcomes of the cell culture experiment are described in Figure 6. The histogram  
144 in Figure 6a outlines the total number of events over a 20-second span. Each histogram peak corresponds to an extracellular  
145 field potential wave. The cells exhibit a beating frequency of 67 bpm. A deeper dive into two histogram peaks is presented in  
146 Figure 6b. Specifically, it shows UP and DN events for each electrode generated by two distinct field potential waves. Each  
147 wave signal has a consistent origin and propagation pattern, resulting in similar footprints in the event space.

148 Figure 6c extracts the wave propagation velocity based on the spatial location of the electrode and the timing of the events  
149 generated. The extracted propagation velocity is 0.11 mm/ms. Finally, a confocal microscope was used to validate the viability  
150 of the tissue and ensure that the extracted beating frequency was correct. A snapshot from the microscope is shown in figure 6d,  
151 where the cell nuclei (in blue) and the cytoskeleton (in red) are highlighted.

152 Expanding upon these results, Figure 7 provides a wealth of information that delves deeper into the propagation of electrical  
153 activity. It graphically presents a time series of the events sensed in response to an extracellular field potential wave as it  
154 travels across the entire array. Each detected wave follows a consistent trajectory, originating from the array's lower right and  
155 culminating at its upper left (also shown in Figure 6b). Crucially, a wave of DN events is succeeded by a wave of UP events.  
156 This sequence mirrors the biphasic dynamics characteristic of EFPs. An additional graphical representation of the data and  
157 further analysis are available in the supplementary material section 5 and 6.

158 In terms of data efficiency, the average unfiltered event rate output from the 4096 GAIA channels amounts to 10 kevs,  
159 signifying a dramatic reduction when compared to conventional sampling methods that can require up to 200 kbps per channel.  
160 This stands as a testament to GAIA's capability of compressing large amounts of data into manageable streams.

## 161 Spiking neural network interfacing

162 GAIA's production of a wholly novel type of data enables an array of exciting possibilities. Building on the results presented, we  
163 successfully interfaced GAIA's event-based outputs to an event-based mixed-signal neuromorphic processor. This integration  
164 aims to harness the benefits of both hardware components, laying the groundwork for their potential unification into a singular  
165 monolithic system. Here, pixel and neuron computations occur in the analog domain, while spike routing is managed digitally.

166 The union of GAIA's advantages with the real-time analysis capabilities of neuromorphic processors promises significant  
167 advancements in the realm of hardware-based neural computation. While several existing neuromorphic processors could  
168 serve as a proof-of-concept [15, 16, 38, 39], we elected to employ the mixed-signal DYNAP-SE [14] processor (described in  
169 Supplementary material section 7) to demonstrate a fully mixed-signal processing pipeline. The analog properties of silicon  
170 neurons and synapses have been extensively described [40–42]. So here we focus on two system-level network motifs. The  
171 first network is a spike detection motif that uses a single analog silicon neuron to detect spikes from a single GAIA channel.  
172 It relies on the integration of UP and DN events through different excitatory input synapses to create coincidence detection  
173 filters [43]. Digital UP events are integrated via NMDA-like silicon synapses, while digital DN events are integrated via  
174 AMPA-like silicon synapses [44]. Both synapses are emulated via dedicated circuits on the DYNAP-SE processor. As in their



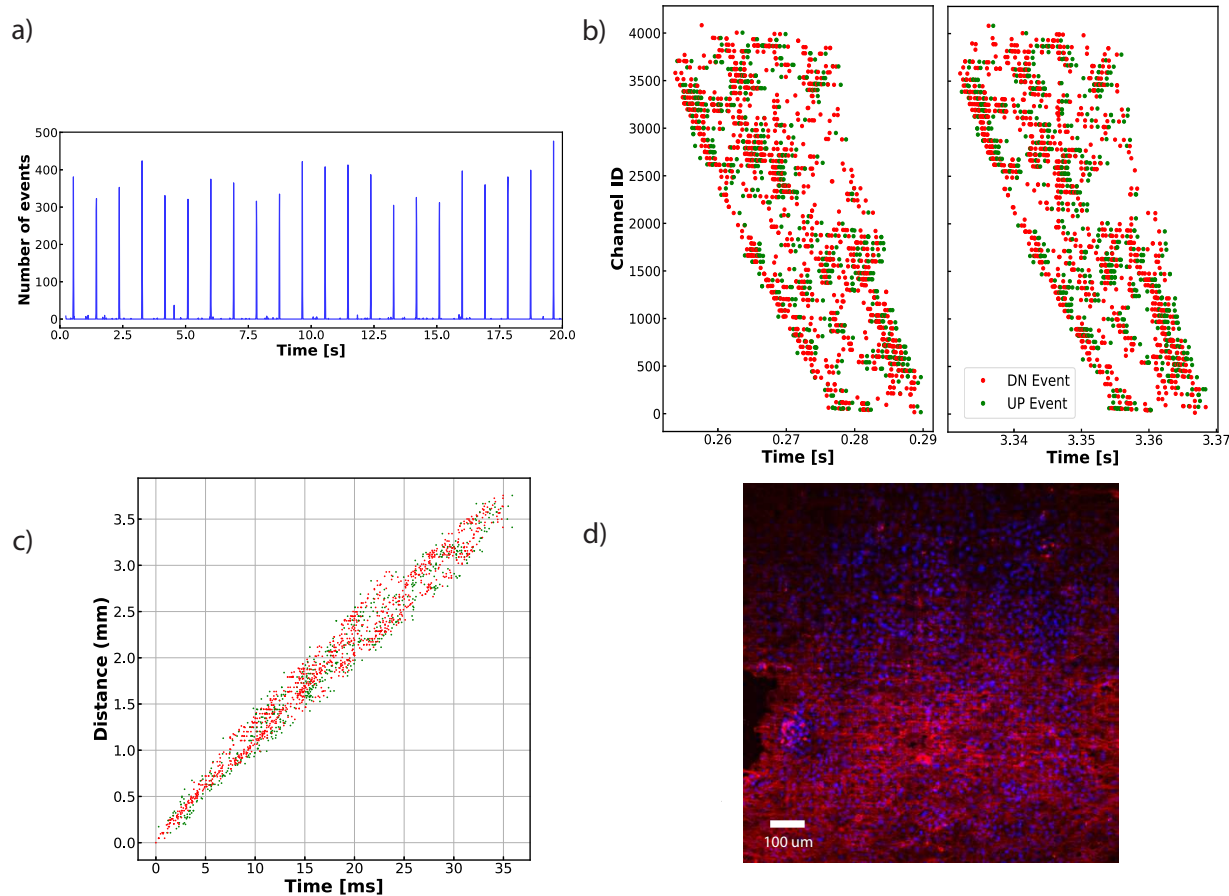


**Figure 6. Analysis and Visualization of Cardiomyocyte Activity on GAIA Sensor.** **a**, Histogram showcasing the event distribution from GAIA over a 20s duration. Periodic peaks, resulting from the spontaneous beating of the CMs, reveal a frequency of 67 bpm. Each peak represents the extracellular field potential in response to a beat event. **b**, Illustration of two distinct beating events. The x-axis represents time and the y-axis indicates the Channel ID, emphasizing the clear signal propagation. Uniformity in the recorded beating shapes indicates the signal's consistent origin and propagation pattern. **c**, Estimation of the propagation speed of the extracellular field potentials, with an estimated velocity of 0.11 mm/ms. **d**, Confocal imaging of cardiomyocyte cell culture on the GAIA sensor. Cytoskeletons in red are stained with SIR-Actin, while cell nuclei in blue are stained with NucBlue, Hoechst 33342. Imaging proves cell viability and optically validates the measured beating frequency.

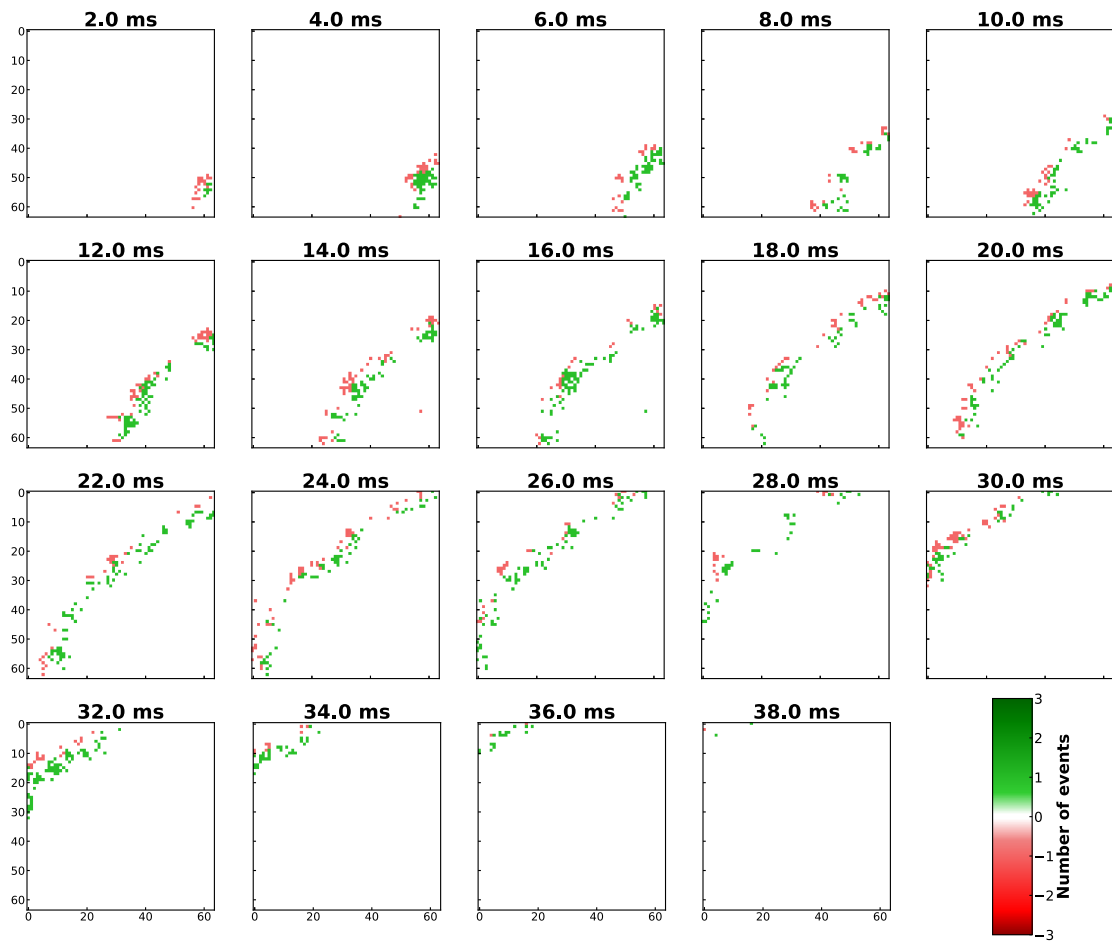


**Figure 7. Propagation of extracellular field potential (EFP) wave.** Time surface showing the propagation of electrical activity from a single EFP wave across the entirety of the GAIA chip. The activity is calculated over a 2 ms time window with an exponential decay parameterized by  $\tau = 2ms$ . Negative and positive events (in red and green) are encoded from the biphasic shape. Notably, within the time frames presented, the total counts for UP and DN events are 1130 and 1111, respectively. Although it might seem that there are more UP events, this is because they represent the trailing edge of the wave, thus occurring closer to the snapshot time, making them appear more prevalent.

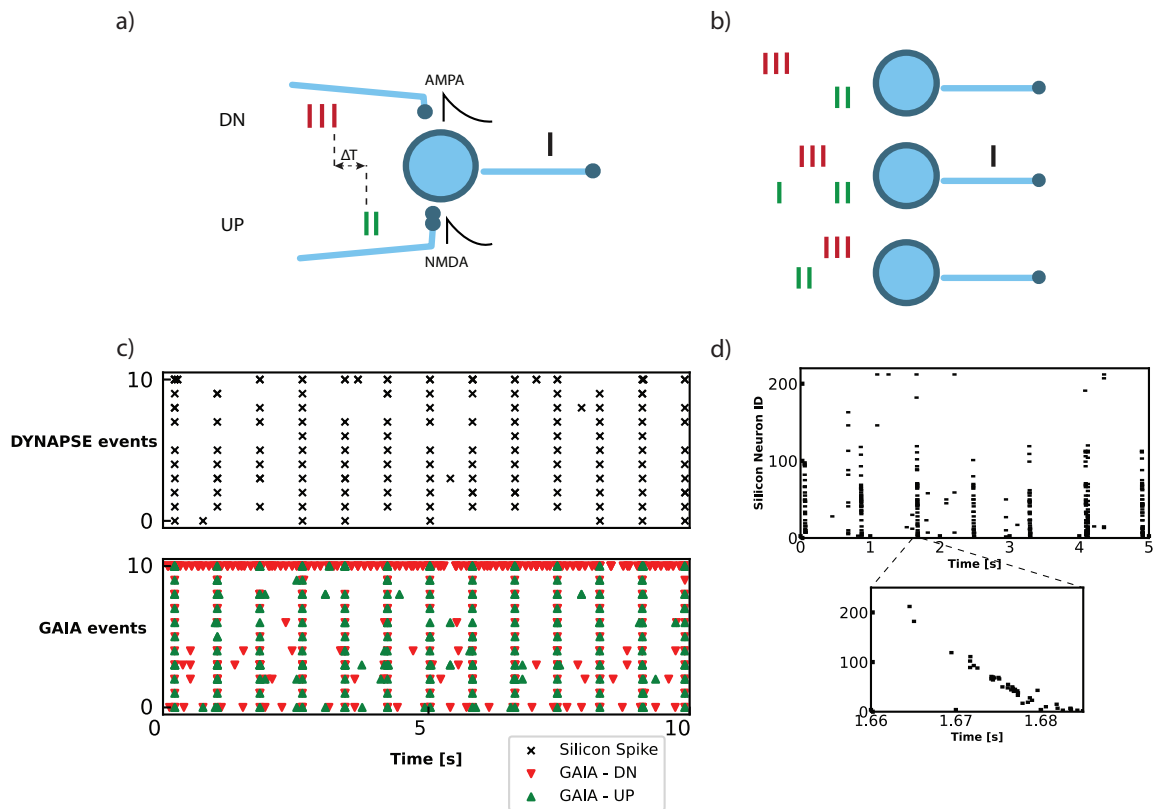


**Figure 8. GAIA - DYNAP-SE interface.** **a**, Spike detection motif. UP and DN channels are connected to different synapses, filtering the incoming digital spikes with different time constants. **b**, The network is tuned to respond only when a sequence with the correct polarity and the correct timing is presented (middle). If the timing (top) or the polarity is inverted (bottom), the silicon neuron is silenced. **c**, Raw GAIA events (bottom) are processed by the DYNAP-SE processor (top). The silicon neurons on the DYNAP-SE spike only in response to a close succession of DN-UP GAIA events. **d**, Neuron-IDs of a full DYNAP-SE core responding to raw, noisy input recorded by GAIA.

175 biological counterpart [45], silicon NMDA synapses are voltage-gated circuit blocks wherein the output synaptic current is  
 176 enhanced by the effect of a recent AMPA synaptic event boosting the neuron membrane potential. The resulting non-linear  
 177 synaptic summation mechanism is leveraged in the spike detection network to trigger an output spike only when subsequent  
 178 DN-UP events occur within a short time window. Figures 8a and b show the described spike detection motif and the selectivity  
 179 to spike time and polarity, respectively. Figures 8c shows, on the bottom, the raw, unfiltered data from a subset of GAIA  
 180 channels and, on the top, the DYNAP-SE events generated in response to the data. The coincidence detection between different  
 181 polarity events is a strong de-noising filter on the single output spikes. The on-chip spike detection network successfully  
 182 responds only to close successions of DN-UP events while correctly silencing events due to noise. The second network uses the  
 183 same principle to process the entire GAIA array within a single DYNAP-SE core. To map the full GAIA array into a single  
 184 DYNAP-SE core, we coarse-grained the 4096 pixels into a 16x16 grid. Each grid element was connected to a single analog  
 185 on-chip neuron. The coarse-graining approach allows processing of the entire GAIA MEA within a single core. The synaptic  
 186 biases and the time constants of the synapses and of the neuron have been tuned to ignore the background noise and limit false  
 187 positives. Figure 8d shows the response over time of the DYNAP-SE core. The main panel shows periodic beating, while the  
 188 bottom zoomed-in image focuses on detecting a single EFP wave event. Silicon neurons show a clear progression at the time of  
 189 detection, consistent with the movement of the EFP wave.

### 190 Advantages and drawbacks of GAIA

191 As delineated in Table 1, the performance metrics of the GAIA system are compared to existing state-of-the-art MEA devices,  
 192 providing a comparative perspective. GAIA stands out prominently due to its unique event-based asynchronous nature:  
 193 the output data rate is solely determined by the sensed extracellular activity. The analog pixel electronics combined with  
 194 asynchronous encoding collectively enable superior energy efficiency and reduced latency. However, the intrinsic nature of

	This work	[3]	[5]	[6]	[7]	[1]
<b>Technology</b> [nm]	180	180	180	130	180	90/65
<b>Die size</b> [mm]	5×5	6×8.9	-	19.2×10	12×8.9	32.5×25.1
<b>Pixel pitch</b> [μm]	48	18	25	15	13.5	11.72
<b>No electrodes</b>	4096	19586	65536	16384	59760	236880
<b>No readout-channels</b>	4096	19586	65536	1024	2048	236880/33840
<b>Sampling rate</b>	<1 μs latency	11.6kHz	20kHz	20kHz	20kHz	10/70kHz
<b>Input-referred noise</b>	19.04	10.4	26	7.5	2.5	5.5
[μV <sub>RMS</sub> ]	(500-3kHz)	(300-5kHz)	(100-10kHz)	(100-3 kHz)	(300-10kHz)	(300–10kHz)
<b>Power/channel</b> [μW]	0.8	5.9	-	19.8	42	130

**Table 1.** Comparison to state-of-the-art MEA systems

asynchronous event-based systems renders time-multiplexing unfeasible, and requires dedicated circuitry at each pixel. This poses a challenge in achieving an optimal balance between electronics size, which influences overall noise levels, and the physical spacing between electrodes, which dictates spatial resolution.

Building upon the architecture of GAIA, its event-based design offers expansive opportunities for scalability. The inherent strength of signal compressing at the pixel level, of the arbiter design, combined with its efficient bandwidth, suggests that the present 64x64 configuration could seamlessly evolve into larger pixel arrays, echoing advances seen in vision sensors [46]. However, it is vital to acknowledge inherent challenges: with the pixel’s active design, transmitting digital data over extended wire lengths within an analog computational environment introduces vulnerabilities to noise disturbances and potential coupling issues.

## Discussion

As traditional multichannel biosensors follow a synchronous clocked data sampling scheme, they are limited in the number of channels they can record from simultaneously due to fundamental bandwidth and power constraints. The work we presented here bridges the gap between direct extracellular sensing and event-based technology, offering a new approach for real-time bioelectric sensing and monitoring. The GAIA sensor proposed evolves classical MEA designs by harnessing event-based encoding, offering benefits such as enhanced energy efficiency and improved scalability. Each pixel asynchronously converts the detected extracellular potential into a stream of digital events. GAIA significantly reduces redundant data at the pixel level, by initiating data generation and transmission only upon significant signal changes, such as single action potentials or large extracellular field potentials. This, in turn, eases the strain on data management and processing frameworks.

Another notable achievement of this paper is the demonstration of an integrated event-based MEA device with a mixed-signal neuromorphic processor. This combination demonstrates the practicality of combining event-based biosensing with neuromorphic processing, suggesting a roadmap for future edge biosensing applications.

The findings and developments presented in this paper set the stage for further exploration in the MEA and biosensor sector. Event-based technology in this context opens new avenues for research and optimization. Moreover, as showcased by direct sensing and processing integration, the potential for edge devices paves the way for more decentralized, efficient, and real-time solutions.

In summary, this work presents a novel technological approach and offers a practical blueprint for the next generation of bioelectronic interfaces, emphasizing real-world applicability and efficiency.

## Methods

### IC Fabrication

The chip was fabricated using a standard 180 nm CMOS 6M1P process. Information on transistor sizing is available in the supplementary materials section 2. The dies were wire-bonded onto custom-made printed circuit boards (PCBs) for effective integration. PCBs were designed using the open-source Kicad software.

### Post-processing, packaging, and Pt-Black deposition

For biocompatibility and usability, a three-phase post-fabrication protocol was employed. First, the chips were post-processed in a cleanroom to fabricate stable platinum electrodes and to isolate the electronics from the culturing media. The GAIA CMOS chip was post-processed at the die level. Platinum electrodes were manufactured on the electrode array using a shifted-electrode

231 layout [47]. Three masks were used to deposit a  $SiO_2/Si_3N_4$  passivation stack over the entire chip. Reactive-ion etching was  
232 used to create openings in the passivation to create the final  $15 \times 15 \mu m^2$  electrodes and for the wire bonding contacts.

233 Secondly, the chips were packaged with epoxy and a glass ring to ensure adequate insulation and to avoid leakage of  
234 the culturing media. Finally, Pt-black was deposited on the bright Pt electrode surface following a previously published  
235 protocol [48]. All electrodes were connected, and a static current of 500uA was applied for 40 s.

### 236 Data Pipeline

237 An XEM7310 FPGA (Opal Kelley, USA) board was used to interface the GAIA chip. Custom drivers were developed in System  
238 Verilog to digitize, timestamp, and pipeline incoming events. Custom C++ software was built to visualize and process incoming  
239 digital events. The same software controls the analog biases and digital latches on the GAIA chip. Additional information is  
240 available in the supplementary material section 3.

### 241 Data Filtering

242 The recorded raw data was filtered to extract salient features by leveraging the analysis performed in figure 5f. The data was  
243 filtered using the event-based algorithms described in algorithm 1.

---

#### Algorithm 1 Event Validation

---

- $E$ : The list of events to be processed.
- $e.ts$ : Timestamp of event  $e$ .
- $e.p$ : Polarity of event  $e$ . Negative and positive polarity are denoted as -1 and 1, respectively.

```
1: for each  $e$  in  $E$  do
2:   if  $\exists e' \in E$  such that  $|e'.ts - e.ts| \leq 1 \text{ ms}$  and  $p.e' = -p.e$  then
3:      $E_{\text{valid}} = E_{\text{valid}} \cup e, e'$  .
4:   else
5:     Discard  $e$  from  $E$ .
6:   end if
7: end for
8: return  $E_{\text{valid}}$ 
```

---

### 244 Characterization setup

245 The chip characterization was conducted using an array of specialized instruments. The transfer function of the A1-A2  
246 amplification chain was assessed using an Agilent Analog Discovery 2. An SRS SR780 network signal analyzer was used  
247 to evaluate the noise and capture the power spectral density measurements. The necessary waveforms for testing were  
248 produced using the Agilent 33120A waveform generator, and their characteristics were monitored using the Agilent DSO6054A  
249 oscilloscope. The chip's analog and digital power needs were met using two separate Hewlett Packard E3610A power supplies.  
250 As for estimating the chip's total power consumption, initial computations were made using the post-layout extraction feature.  
251 These preliminary estimates were validated using real-time readings from the aforementioned power supplies.

### 252 Cell Culture

253 Frozen vials of human-derived cardiomyocytes (iCell Cardiomyocytes Kit (Cat. R1057)) were purchased from Fujifilm Cellular  
254 Dynamics International (Wisconsin, USA). The cells were thawed and cultured following the manufacturer's guidelines. Before  
255 cell plating, the GAIA sensors were sterilized in 70% ethanol for 10 minutes and rinsed thrice with sterile deionized water.  
256 The electrode arrays were coated with human fibronectin (Cat. FC010, Sigma-Aldrich) at a concentration of 50 mg/mL and  
257 incubated at 37 °C for 1 hour. The cells underwent a thawing procedure and had seeding density adjusted [37, 49]. 30000  
258 cells were seeded onto the fibronectin-coated GAIA sensors, and 1.3 mL of iCell Plating Medium was added to each chamber.  
259 After 48 hours, iCell Plating Medium was fully replaced with 1.3 mL iCell Maintenance Medium. Half of the medium was  
260 exchanged using iCell Maintenance Medium every 2-3 days until the termination of the experiments.

## References

1. Kato, Y., Matoba, Y., Honda, K., Ogawa, K., Shimizu, K., Maehara, M., Fujiwara, A., Odawara, A., Yamane, C., Kimizuka, N., *et al.* High-Density and Large-Scale MEA System Featuring 236,880 Electrodes at 11.72  $\mu\text{m}$  Pitch for Neuronal Network Analysis in 2020 IEEE Symposium on VLSI Circuits (2020), 1–2.
2. Sahasrabudde, K., Khan, A. A., Singh, A. P., Stern, T. M., Ng, Y., Tadić, A., Orel, P., LaReau, C., Pouzner, D., Nishimura, K., *et al.* The Argo: a high channel count recording system for neural recording in vivo. *Journal of neural engineering* **18**, 015002 (2021).
3. Yuan, X., Hierlemann, A. & Frey, U. Extracellular Recording of Entire Neural Networks Using a Dual-Mode Microelectrode Array With 19 584 Electrodes and High SNR. *IEEE Journal of Solid-State Circuits* **56**, 2466–2475 (2021).
4. Müller, J., Ballini, M., Livi, P., Chen, Y., Radivojevic, M., Shadmani, A., Viswam, V., Jones, I. L., Fiscella, M., Diggelmann, R., *et al.* High-resolution CMOS MEA platform to study neurons at subcellular, cellular, and network levels. *Lab on a Chip* **15**, 2767–2780 (2015).
5. Tsai, D., Sawyer, D., Bradd, A., Yuste, R. & Shepard, K. L. A very large-scale microelectrode array for cellular-resolution electrophysiology. *Nature Communications* **8**, 1802 (2017).
6. Lopez, C. M., Chun, H. S., Wang, S., Berti, L., Putzeys, J., Van Den Bulcke, C., Weijers, J.-W., Firrincieli, A., Reumers, V., Braeken, D., *et al.* A multimodal CMOS MEA for high-throughput intracellular action potential measurements and impedance spectroscopy in drug-screening applications. *IEEE Journal of Solid-State Circuits* **53**, 3076–3086 (2018).
7. Dragas, J., Viswam, V., Shadmani, A., Chen, Y., Bounik, R., Stettler, A., Radivojevic, M., Geissler, S., Obien, M. E. J., Müller, J., *et al.* In vitro multi-functional microelectrode array featuring 59 760 electrodes, 2048 electrophysiology channels, stimulation, impedance measurement, and neurotransmitter detection channels. *IEEE journal of solid-state circuits* **52**, 1576–1590 (2017).
8. Donati, E. & Indiveri, G. Neuromorphic bioelectronic medicine for nervous system interfaces: from neural computational primitives to medical applications. *Progress in Biomedical Engineering* **5**, 013002. ISSN: 2516-1091. <http://dx.doi.org/10.1088/2516-1091/acb51c> (Jan. 2023).
9. Lichtsteiner, P., Posch, C. & Delbruck, T. A 128x128 120 dB 15  $\mu\text{s}$  Latency Asynchronous Temporal Contrast Vision Sensor. *IEEE Journal of Solid-State Circuits* **43**, 566–576. ISSN: 0018-9200 (Feb. 2008).
10. Liu, S., van Schaik, A., Minch, B. & Delbruck, T. Event-based 64-channel binaural silicon cochlea with Q enhancement mechanisms in Circuits and Systems (ISCAS), *Proceedings of 2010 IEEE International Symposium on* (2010), 2027–2030.
11. Sarpeshkar, R., Lyon, R. F. & Mead, C. in *Neuromorphic systems engineering* 49–103 (Springer, 1998).
12. Caviglia, S., Pinna, L., Valle, M. & Bartolozzi, C. Spike-Based Readout of POSFET Tactile Sensors. *IEEE Transactions on Circuits and Systems I: Regular Papers* **64**, 1421–1431 (2017).
13. Bartolozzi, C., Indiveri, G. & Donati, E. Embodied neuromorphic intelligence. *Nature Communications* **13**. ISSN: 2041-1723. <http://dx.doi.org/10.1038/s41467-022-28487-2> (Feb. 2022).
14. Moradi, S., Qiao, N., Stefanini, F. & Indiveri, G. A Scalable Multicore Architecture With Heterogeneous Memory Structures for Dynamic Neuromorphic Asynchronous Processors (DYNAPs). *IEEE Transactions on Biomedical Circuits and Systems* **12**, 106–122 (Feb. 2018).
15. Davies, M., Srinivasa, N., Lin, T.-H., Chinya, G., Cao, Y., Choday, S. H., Dimou, G., Joshi, P., Imam, N., Jain, S., Liao, Y., Lin, C.-K., Lines, A., Liu, R., Mathaikutty, D., McCoy, S., Paul, A., Tse, J., Venkataramanan, G., Weng, Y.-H., Wild, A., Yang, Y. & Wang, H. Loihi: A neuromorphic manycore processor with on-chip learning. *IEEE Micro* **38**, 82–99 (2018).
16. Furber, S., Galluppi, F., Temple, S. & Plana, L. The SpiNNaker Project. *Proceedings of the IEEE* **102**, 652–665. ISSN: 0018-9219 (May 2014).
17. Pehle, C., Billaudelle, S., Cramer, B., Kaiser, J., Schreiber, K., Stradmann, Y., Weis, J., Leibfried, A., Müller, E. & Schemmel, J. The BrainScaleS-2 Accelerated Neuromorphic System With Hybrid Plasticity. *Frontiers in Neuroscience* **16**. ISSN: 1662-453X. <https://www.frontiersin.org/articles/10.3389/fnins.2022.795876> (2022).
18. Xu, Y., De la Paz, E., Paul, A., Mahato, K., Sempionatto, J. R., Tostado, N., Lee, M., Hota, G., Lin, M., Uppal, A., *et al.* In-ear integrated sensor array for the continuous monitoring of brain activity and of lactate in sweat. *Nature Biomedical Engineering*, 1–14 (2023).
19. Chen, G., Cao, H., Conradt, J., Tang, H., Rohrbein, F. & Knoll, A. Event-based neuromorphic vision for autonomous driving: A paradigm shift for bio-inspired visual sensing and perception. *IEEE Signal Processing Magazine* **37**, 34–49 (2020).

- 311 20. Haessig, G., Milde, M. B., Aceituno, P. V., Oubari, O., Knight, J. C., van Schaik, A., Benosman, R. B. & Indiveri, G.  
312 Event-Based Computation for Touch Localization Based on Precise Spike Timing. *Frontiers in Neuroscience* **14**, 420.  
313 ISSN: 1662-453X. <https://www.frontiersin.org/article/10.3389/fnins.2020.00420> (2020).
- 314 21. Yokouchi, T., Sugimoto, S., Rana, B., Seki, S., Ogawa, N., Shiomi, Y., Kasai, S. & Otani, Y. Pattern recognition with  
315 neuromorphic computing using magnetic field-induced dynamics of skyrmions. *Science Advances* **8**, eabq5652. eprint:  
316 <https://www.science.org/doi/pdf/10.1126/sciadv.abq5652>. <https://www.science.org/doi/abs/10.1126/sciadv.abq5652> (2022).
- 318 22. Donati, E., Payvand, M., Risi, N., Krause, R. & Indiveri, G. Discrimination of EMG Signals Using a Neuromorphic  
319 Implementation of a Spiking Neural Network. *Biomedical Circuits and Systems, IEEE Transactions on* **13**, 795–803  
320 (2019).
- 321 23. Göltz, J., Kriener, L., Baumbach, A., Billaudelle, S., Breitwieser, O., Cramer, B., Dold, D., Kungl, A. F., Senn, W.,  
322 Schemmel, J., *et al.* Fast and energy-efficient neuromorphic deep learning with first-spike times. *Nature machine*  
323 *intelligence* **3**, 823–835 (2021).
- 324 24. Indiveri, G. & Sandamirskaya, Y. The importance of space and time for signal processing in neuromorphic agents. *IEEE*  
325 *Signal Processing Magazine* **36**, 16–28 (2019).
- 326 25. Boahen, K. Point-to-Point Connectivity Between Neuromorphic Chips Using Address-Events. *IEEE Transactions on*  
327 *Circuits and Systems II: Analog and Digital Signal Processing* **47**, 416–34 (2000).
- 328 26. Kassiri, H., Abdelhalim, K. & Genov, R. *Low-distortion super-GOhm subthreshold-MOS resistors for CMOS neural*  
329 *amplifiers in 2013 IEEE Biomedical Circuits and Systems Conference (BioCAS)* (2013), 270–273.
- 330 27. Corradi, F., You, H., Giulioni, M. & Indiveri, G. *Decision making and perceptual bistability in spike-based neuromorphic*  
331 *VLSI systems in International Symposium on Circuits and Systems (ISCAS)* (2015), 2708–2711.
- 332 28. Lazzaro, J., Wawrzynek, J., Mahowald, M., Sivilotti, M. & Gillespie, D. Silicon auditory processors as computer  
333 peripherals. *IEEE Transactions on Neural Networks* **4**, 523–528 (1993).
- 334 29. Mahowald, M. The Silicon Retina. *Scientific American* **264**, 76–82 (1991).
- 335 30. Miskowicz, M. Send-on-delta concept: An event-based data reporting strategy. *sensors* **6**, 49–63 (2006).
- 336 31. Liu, Q., Richter, O., Nielsen, C., Sheik, S., Indiveri, G. & Qiao, N. *Live demonstration: Face recognition on an ultra-low*  
337 *power event-driven convolutional neural network ASIC in IEEE Computer Society Conference on Computer Vision and*  
338 *Pattern Recognition Workshops 2019-June* (2019). ISBN: 9781728125060.
- 339 32. Boahen, K. A Burst-Mode Word-Serial Address-Event Link – I: Transmitter Design. *IEEE Transactions on Circuits and*  
340 *Systems I* **51**, 1269–80 (2004).
- 341 33. Mitra, S., Indiveri, G. & Fusi, S. *Learning to classify complex patterns using a VLSI network of spiking neurons in*  
342 *Advances in Neural Information Processing Systems (NIPS)* (eds Platt, J., Koller, D., Singer, Y. & Roweis, S.) **20** (MIT  
343 Press, Cambridge (MA), 2008), 1009–1016.
- 344 34. Lazar, A. A., Pnevmatikakis, E. A. & Zhou, Y. The power of connectivity: identity preserving transformations on visual  
345 streams in the spike domain. *Neural networks* **44**, 22–35 (2013).
- 346 35. SPACH, M. S., BARR, R. C., JOHNSON, E. A. & KOOTSEY, J. M. Cardiac extracellular potentials: analysis of complex  
347 wave forms about the Purkinje networks in dogs. *Circulation research* **33**, 465–473 (1973).
- 348 36. DeBusschere, B. & Kovacs, G. T. Portable cell-based biosensor system using integrated CMOS cell-cartridges. *Biosensors*  
349 *and Bioelectronics* **16**, 543–556. ISSN: 0956-5663 (2001).
- 350 37. Lee, J., Ganswein, T., Ulsan, H., Emmenegger, V., Saguner, A. M., Duru, F. & Hierlemann, A. Repeated and On-Demand  
351 Intracellular Recordings of Cardiomyocytes Derived from Human-Induced Pluripotent Stem Cells. *ACS sensors* **7**, 3181–  
352 3191 (2022).
- 353 38. Thakur, C. S., Molin, J. L., Cauwenberghs, G., Indiveri, G., Kumar, K., Qiao, N., Schemmel, J., Wang, R., Chicca, E.,  
354 Olson Hasler, J., Seo, J.-s., Yu, S., Cao, Y., van Schaik, A. & Etienne-Cummings, R. Large-Scale Neuromorphic Spiking  
355 Array Processors: A Quest to Mimic the Brain. *Frontiers in Neuroscience* **12**, 891. <https://www.frontiersin.org/article/10.3389/fnins.2018.00891> (2018).
- 357 39. Richter, O., Wu, C., Whatley, A. M., Köstinger, G., Nielsen, C., Qiao, N. & Indiveri, G. DYNAP-SE2: a scalable multi-core  
358 dynamic neuromorphic asynchronous spiking neural network processor. *arXiv preprint arXiv:2310.00564* (2023).

- 359 40. Indiveri, G., Chicca, E. & Douglas, R. A VLSI array of low-power spiking neurons and bistable synapses with spike-timing  
360 dependent plasticity. *IEEE Transactions on Neural Networks* **17**, 211–221 (Jan. 2006).
- 361 41. Chicca, E., Stefanini, F., Bartolozzi, C. & Indiveri, G. Neuromorphic electronic circuits for building autonomous cognitive  
362 systems. *Proceedings of the IEEE* **102**, 1367–1388. ISSN: 0018-9219 (Sept. 2014).
- 363 42. Bartolozzi, C. & Indiveri, G. *A selective attention multi-chip system with dynamic synapses and spiking neurons* in  
364 *Advances in Neural Information Processing Systems (NIPS)* (eds Schölkopf, B., Platt, J. & Hofmann, T.) **19** (MIT Press,  
365 Cambridge, MA, USA, Dec. 2007), 113–120.
- 366 43. Buhusi, C. V., Oprisan, S. A. & Buhusi, M. Clocks within clocks: timing by coincidence detection. *Current opinion in*  
367 *behavioral sciences* **8**, 207–213 (2016).
- 368 44. Koch, C. & Segev, I. *Methods in neuronal modeling: from ions to networks* (MIT press, 1998).
- 369 45. Gómez González, J. F., Mel, B. W. & Poirazi, P. Distinguishing linear vs. non-linear integration in CA1 radial oblique  
370 dendrites: it's about time. *Frontiers in computational neuroscience* **5**, 44 (2011).
- 371 46. Guo, M., Chen, S., Gao, Z., Yang, W., Bartkovjak, P., Qin, Q., Hu, X., Zhou, D., Uchiyama, M., Fukuoka, S., *et al.* *A*  
372 *3-Wafer-Stacked hybrid 15MPixel CIS+ 1 MPixel EVS with 4.6 GEvent/s readout, In-Pixel TDC and On-Chip ISP and*  
373 *ESP function* in *2023 IEEE International Solid-State Circuits Conference (ISSCC)* (2023), 90–92.
- 374 47. Heer, F., Franks, W., Blau, A., Taschini, S., Ziegler, C., Hierlemann, A. & Baltes, H. CMOS microelectrode array for the  
375 monitoring of electrogenic cells. *Biosensors and Bioelectronics* **20**, 358–366 (2004).
- 376 48. Ronchi, S., Fiscella, M., Marchetti, C., Viswam, V., Müller, J., Frey, U. & Hierlemann, A. Single-Cell Electrical  
377 Stimulation Using CMOS-Based High-Density Microelectrode Arrays. *Frontiers in Neuroscience* **13**. ISSN: 1662-453X.  
378 <https://www.frontiersin.org/articles/10.3389/fnins.2019.00208> (2019).
- 379 49. Zhao, M., Tang, Y., Zhou, Y. & Zhang, J. Deciphering role of Wnt signalling in cardiac mesoderm and cardiomyocyte  
380 differentiation from human iPSCs: four-dimensional control of Wnt pathway for hiPSC-CMs differentiation. *Scientific*  
381 *reports* **9**, 19389 (2019).

## 382 Acknowledgements

383 The authors thank Tugba Demirci, Charlotte Frenkel, Peter Rimpf, Jihyun Lee, Xiaohan Xue, Jana Petr, and Jonathan Schmidli  
384 for their support throughout the project. This work was supported by the Swiss National Science Foundation (SNSF) project  
385 205320\_188910/1, SNSF Sinergia project CRSII5-180316, and UZH Candoc FK-22-084.

## 386 Author contributions statement

387 M.C. G.H. F.Ca. and G.I. conceived the project direction and experiments. M.C. S.N. F.Ca. and H.U. designed the GAIA  
388 sensor. M.C. designed the PCBs and the interfacing firmware. M.C. and N.R. developed the FPGA firmware. M.C. F.Ca. and  
389 H.U. were involved in the post-processing biocompatibility steps. M.C. C.-V.H.B. F.Ca. and H.U. conducted the cell culture  
390 experiments. M.C. analyzed the data. M.C. F.Co. and N.R. developed the on-chip SNN. G.I. A.H. and F.Ca. supervised the  
391 project in general. M.C. wrote the manuscript with inputs and revisions from all authors.

## 392 Additional information

393 **Competing interests** The authors declare that they have no competing interests at the time of submission.

394 **Supplementary information** is available at XX.

395 **Corresponding authors** M.C. and G.I. are the corresponding authors.



## Supplementary Files

This is a list of supplementary files associated with this preprint. Click to download.

- [GAIAsuppvideoEFPpropagationfast.gif](#)
- [GAIAsuppvideoEFPpropagationslow.gif](#)
- [GAIASM.pdf](#)